Effect of nonstoichiometry on the transition from ferromagnetism to antiferromagnetism in the ternary indides $Ce_{1.95}Pd_{2+2x}In_{1-x}$ and $Ce_{2+x}Pd_{1.85}In_{1-x}$

M. Giovannini
Dipartimento di Chimica e Chimica Industriale, Università di Genova, Via Dodecaneso 31, I-16146 Genova, Italy

H. Michor, E. Bauer, and G. Hilscher
Institut für Experimentalphysik, TU Wien, Wiedner Hauptstrasse 8-10, A-1040 Wien, Austria

P. Rogl
Institut für Physikalische Chemie, Universität Wien, Währingerstrasse 42, A-1090 Wien, Austria

T. Bonelli, F. Fauth, P. Fischer, T. Herrmannsdörfer, and L. Keller
Laboratory for Neutron Scattering, ETH Zürich & Paul Scherrer Institute, CH-5232 Villigen-PSI, Switzerland

W. Sikora
The Faculty of Physics and Nuclear Techniques, The University of Mining and Metallurgy, PL-30-059 Krakow, Poland

A. Saccone and R. Ferro
Dipartimento di Chimica e Chimica Industriale, Università di Genova, Via Dodecaneso 31, I-16146 Genova, Italy

(Received 26 July 1999)

Single phase polycrystalline samples of the ternary indides $Ce_{1.95}Pd_{2+2x}In_{1-x}$ ($0.05 \leqslant x \leqslant 0.23$) and $Ce_{2+x}Pd_{1.85}In_{1-x}$ ($0.06 \leqslant x \leqslant 0.37$) were synthesized and characterized by microprobe analysis and x-ray diffraction. The effect of the chemical composition on the magnetic properties was investigated by means of magnetization and specific-heat measurements as well as by neutron diffraction. The ternary indides crystallize in the parent Mo_2FeB_2 structure (space group $P4/mbm$) and form two branches of solid solutions due to different substitutional mechanisms. In the Pd-rich branch indium vacancies at the $2a$ site are compensated by an excess of palladium located at an additional $4e$ site. In the Ce-rich branch the excess of cerium replaces indium atoms at the $2a$ site. The magnetic properties are strongly influenced by the chemical composition. Excess of palladium favors antiferromagnetism of a sinusoidal modulated type with the propagation vector $\mathbf{k} \approx [0.22,0,0]$, whereas excess of cerium induces ferromagnetism. The magnetic moments in both cases are oriented parallel to the $\mathbf{c}$ axis.

I. INTRODUCTION

Several ternary compounds with the formula Ce_2T_2X (T=transition metal and X=In or Sn) have recently been investigated and some of them exhibit interesting properties such as dense Kondo or heavy fermion behavior.[1–5] The compounds derived from the formula Ce_2Pd_2X, with X=In and Sn, are characterized by an extended solid solubility and their magnetic properties are critically influenced by the chemical composition. The solid solution of the ternary stannides, of a new structure type derived from the tetragonal Mo_2FeB_2 type, was investigated by Laffargue *et al.*,[6] Fourgeot *et al.*,[7] and Gordon and DiSalvo.[8] According to the first two groups of authors the homogeneity range of this compound is of the form $Ce_2Pd_{2+x}Sn_{1-x}$ with $0.04 \leqslant x \leqslant 0.21$. Two magnetic transitions are observed close to the 2:2:1 stoichiometry, whereas only antiferromagnetic order is detected in the Pd-rich area of the solid solution. These results are in partial contradiction to those of Gordon and DiSalvo.[8] The region of the solid solution is supposed to be of triangular shape. Moreover, Ce_2Pd_2Sn is reported by Gordon *et al.*[3] to exhibit simple ferromagnetic order.

Gordon *et al.*[3] and later Fourgeot *et al.*[7] noticed also for the homologous ternary indides an extensive homogeneity range but, whereas Gordon measured the magnetic susceptibility only above 4.2 K revealing just the ferromagnetic transition, the second group of authors observed that $Ce_2Pd_{2.06}Sn_{0.94}$ and $Ce_2Pd_{2.04}In_{0.96}$ exhibit a similar magnetic behavior at low temperatures, both alloys showing two magnetic transitions.

For a thorough investigation of this subject, we explored the homogeneity range of the ternary indides with samples of selected composition with respect to electron microprobe, x-ray diffraction, and magnetic measurements. In $Ce_2Pd_{2.04}Sn_{0.96}$ a change from ferromagnetism at 3.0 K to incommensurate antiferromagnetism at 4.8 K has been observed by Laffargue *et al.* by means of neutron diffraction.[6] The propagation vector $\mathbf{k} = [q,0,0]$ of the sinusoidal modulation varies from $q = 0.075(3)$ at 2.8 K to 0.112(3) at 4.5 K. For the antiferromagnetic configuration no model describing the relation between the magnetic moments at the four Ce sites in the chemical unit cell has been published in Ref. 6.

The aim of this paper is to study the interplay of crystal chemistry and magnetism in the homogeneity range of the ternary indide. Besides magnetic and specific-heat measurements, detailed neutron-diffraction experiments have been

0163-1829/2000/61(6)/4044(10)/$15.00

TABLE I. Microprobe analysis and lattice parameters of the two branches $Ce_{1.95}Pd_{2+2x}In_{1-x}$, $Ce_{2+x}Pd_{1.85}In_{1-x}$, and of some alloys in the neighboring region (all the samples, if not specified otherwise, were annealed for 10 days at $T=750\,°C$).

No.	Nom. comp. [at. %]	EPMA [at. %]	a [nm]	c [nm]	V [nm^3]	Additional phases
	$Ce_{40}Pd_{40}In_{20}$ (Ref. 4)		0.7793(2)	0.3927(1)	0.2385	
	$Ce_{40}Pd_{40}In_{20}$	$Ce_{41}Pd_{40}In_{19}$	0.7806(1)	0.3922(1)	0.2390	CePdIn
		$Ce_{1.95}Pd_{2+2x}In_{1-x}$ branch A				
1	$Ce_{40}Pd_{41}In_{19}$	$Ce_{39}Pd_{42}In_{19}$ [a] ($x=0.05$)	0.7797(1)	0.3928(1)	0.2388	
2	$Ce_{40}Pd_{43}In_{17}$	$Ce_{39}Pd_{44}In_{17}$ ($x=0.10$)	0.7764(3)	0.3962(2)	0.2388	traces $Ce_4Pd_7In_3$
3	$Ce_{40}Pd_{45}In_{15}$	$Ce_{38}Pd_{46}In_{16}$ ($x=0.175$)	0.7747(1)	0.3982(1)	0.2390	traces $Ce_4Pd_7In_3$
4	$Ce_{39}Pd_{48}In_{13}$	$Ce_{39}Pd_{47}In_{14}$ ($x=0.225$)	0.7695(1)	0.4017(1)	0.2379	traces Ce_3Pd_5
		$Ce_{2+x}Pd_{1.85}In_{1-x}$ branch B				
5	$Ce_{42}Pd_{38}In_{20}$	$Ce_{42}Pd_{39}In_{19}$ ($x=0.06$)	0.7813(3)	0.3908(3)	0.2386	traces Ce_3In
6	$Ce_{45}Pd_{35}In_{20}$	$Ce_{44}Pd_{38}In_{18}$ ($x=0.15$)	0.7831(1)	0.3912(3)	0.2394	traces Ce_3In
7	$Ce_{47}Pd_{37}In_{16}$	$Ce_{45}Pd_{39}In_{16}$ ($x=0.22$)	0.7878(2)	0.3914(1)	0.2422	traces Ce_3In
8	$Ce_{50}Pd_{36}In_{14}$	$Ce_{49}Pd_{38}In_{13}$ ($x=0.37$)	0.7911(3)	0.3923(2)	0.2455	traces Ce_3In
9	$Ce_{43}Pd_{44}In_{13}$	$Ce_{41}Pd_{40}In_{19}$				$CePd+Ce_3Pd_4$
10	$Ce_{47}Pd_{42}In_{11}$	$Ce_{44}Pd_{38}In_{18}$				CePd

[a]Annealed for 2 weeks at $T=840\,°C$ in order to homogenize the sample.

performed on the ferromagnetic $Ce_{47}Pd_{37}In_{16}$ sample and the antiferromagnetic $Ce_{40}Pd_{45}In_{15}$ specimen (nominal compositions) both in the paramagnetic and in the magnetically ordered states.

II. EXPERIMENTAL DETAILS

Ingots of palladium (99.9% mass, Metalli Preziosi), indium (99.9% mass, Johnson & Matthey), and cerium (99.9% Auer-Remy) were used as starting elements. The samples, each of a total weight of about 2 g (two samples of about 10 g were prepared for neutron-diffraction measurements), were prepared by argon arc melting or by melting the elements sealed in a tantalum crucible under argon. All the compounds were generally annealed at 750 °C for 10 days.

The details of preparation techniques, x-ray diffraction, magnetic susceptibility, and specific-heat measurements have already been described in a previous paper on R_2Pd_2In (R=rare-earth metal) compounds.[9] Samples for metallographic examination were polished using SiC and diamond pastes; the samples were usually etched in an alcoholic (0.5–1 %) HNO_3 solution. Scanning electron microscopy (SEM) and electron-probe microanalysis (EPMA) based on energy-dispersive x-ray spectroscopy were employed to investigate phase equilibria and phase composition (the pure elements served as standards) and compositional values derived were usually accurate to ± 1 at. %.

Elastic neutron-scattering experiments were performed on the high-resolution diffractometer D1A (neutron wavelength $\lambda_n=0.1911$ nm) and on the high-intensity diffractometers D1B ($\lambda_n=0.252$ nm) at the high-flux reactor of the Institut Laue-Langevin (ILL), Grenoble, and DMC situated at a supermirror coated guide for cold neutrons at the Swiss spallation neutron source SINQ of the Paul Scherrer Institute (PSI) at Villigen ($\lambda_n=0.420$ nm). The powder samples of nominal compositions $Ce_{47}Pd_{37}In_{16}$ (''ferromagnetic'') and $Ce_{40}Pd_{45}In_{15}$ (''antiferromagnetic'') were enclosed, under He gas atmosphere, into cylindrical vanadium tubes of 8- and 9-mm diameter, respectively, and of about 5-cm height. According to the measured neutron transmission, absorption corrections were included in the calculations (product of linear absorption coefficient μ and of sample radius r: $\mu_r=0.176$ and 0.194, respectively, for $\lambda_n=0.1911$ nm). Refinements of the neutron-diffraction data were made by means of the program FULLPROF,[10] using the internal table of neutron-scattering lengths and describing the neutron magnetic form factor of Ce^{3+} in dipole approximation according to the relativistic Dirac-Fock calculations of Freeman and Desclaux.[11]

III. RESULTS AND DISCUSSION

A. The homogeneity region at 750 °C

In the course of the preparation of samples with the composition R_2Pd_2In (R=rare-earth element) and of a parallel investigation of some of the phase equilibria in the ternary system Ce-Pd-In, we found that Ce_2Pd_2In is just on the border of an off-stoichiometric region extending towards deficiency in In.[9]

The homogeneity field of the solid solution (which in the following will be called τ solid solution) was determined by microprobe analysis on several samples in the region close to the 2:2:1 composition. Further samples were prepared within the horseshoe-shaped homogeneity region. The latter samples are nearly single phase although generally traces of another phase appear. Compositions as well as lattice parameters are shown in Table I.

Figure 1 shows the extension of the τ solid solution and the location of some of the samples prepared, together with some indications about the phase relations. Details about the

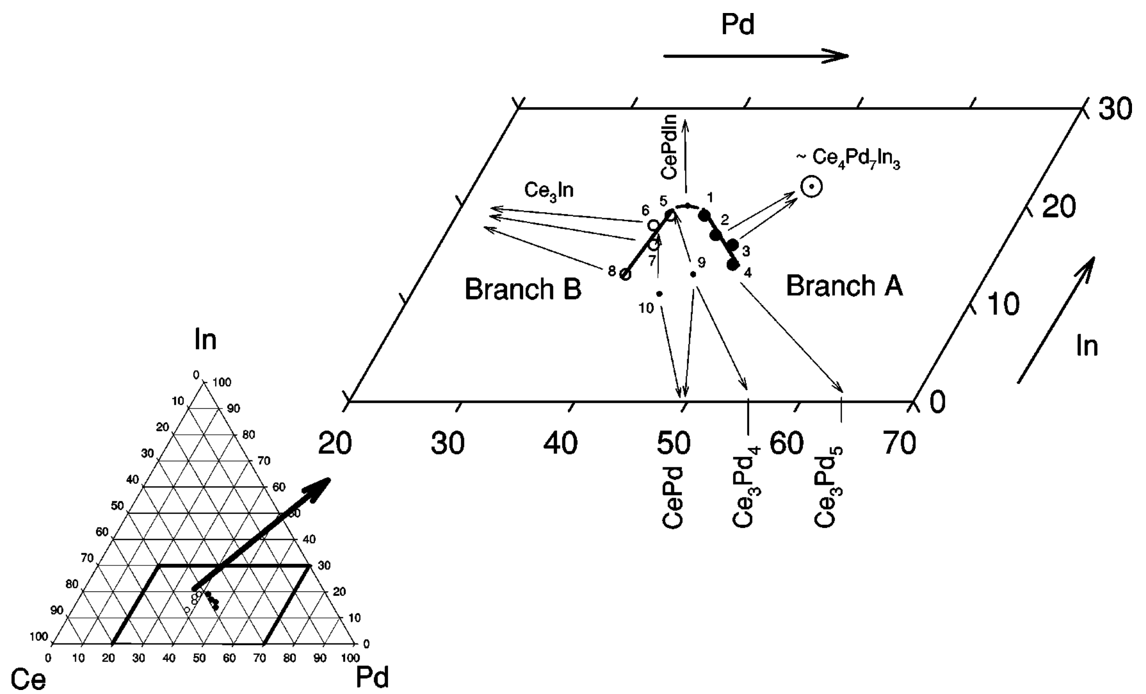

FIG. 1. Location of the two branches (A: $Ce_{1.95}Pd_{2+2x}In_{1-x}$; B: $Ce_{2+x}Pd_{1.85}In_{1-x}$) of the τ solid solution and adjoining phase relations in the ternary phase diagram. A new ternary compound is shown (Ref. 12).

adjoining phase equilibria will be reported elsewhere.[12] The region of the τ solid solution was previously estimated to be roughly triangular[9] but a more detailed investigation of the adjoining equilibria revealed a horseshoelike homogeneity field formed by two branches starting nearby the $Ce_{40}Pd_{40}In_{20}$ composition. One branch extends towards the Pd-rich area up to $Ce_{39}Pd_{47}In_{14}$ (indicated as branch A) and the other (branch B) in the Ce-rich area up to $Ce_{49}Pd_{38}In_{13}$ (see Fig. 1). One sample enclosed within the virtual triangular region and another one located on its proximity indeed resulted to be three and two phase, respectively (they are indicated in Fig. 1 and Table I as sample Nos. 9 and 10). These observations confirm the rather narrow width (ca. 1 at. %) of the branches of the horseshoe-like homogeneity region. Within the accepted error of ± 1 at. %, microprobe data are consistent with the general formula $Ce_{1.95}Pd_{2+2x}In_{1-x}$ for the Pd-rich branch A and the general formula $Ce_{2+x}Pd_{1.85}In_{1-x}$ for the Ce-rich branch B.

The alloy with the stoichiometry 2:2:1 is located in the proximity of the crossover of the "double-branched" solid solution in which two distinct substitutional mechanisms are involved. It is worth noting that at present it was not possible to obtain a sample with the stoichiometric composition 2:2:1 in single phase condition, as already emphasized also by other authors.[7,13] Thus it cannot be excluded that the two branches are in fact disconnected by a very thin two-phase region which encloses the alloy of composition 40% at Ce, 40% at Pd, 20% at In (as suggested in Fig. 1 by a dashed line).

B. Structural chemistry

For the branch A a powder sample of nominal composition $Ce_{40}Pd_{45}In_{15}$ was investigated on D1A at 10 K in the paramagnetic state. Corresponding neutron-diffraction patterns are shown in Fig. 2(a). For the quantitative Rietveld refinement of the neutron powder intensity data, we started from the model of a new derivative structure of the tetragonal U_3Si_2 type, suggested both by Fourgeot[7] and Gordon,[8] in order to explain the excess of Pd in the analogous stannide. Compared to the Mo_2FeB_2 type which was previously assigned for the Ce_2Pd_2In stoichiometry,[1,4,9] in the off-stoichiometric Pd-rich branch In vacancies at the site $2a$ (0, 0, 0) are compensated by the surplus of Pd located at an additional $4e$ site (0, 0, $\approx$0.32). As already stressed by Gordon[8] no interstitial position of considerable size other than that close to the $2a$ site occurs in the Ce_2Pd_2Sn structure. A similar situation may thus be inferred for the homologous Ce_2Pd_2In case.

For the stannide compound ^{119}Sn Mössbauer data[7] seem to confirm an even more sophisticated model where a small amount of additional Sn-atoms was claimed to occupy a $4e$ site (0, 0, 0.068) close to the Sn atoms at the origin (model B of Forgeot). A refinement based on this model, where a small amount of In atoms at the origin was substituted by In atoms in close proximity to the site at the origin [occupation of 10.8% In in $4e$ (0, 0, 0.081)] revealed insignificantly lower R values ($R_B=6.51\%$, $R_F=4.72\%$, $\chi^2=4.08$) when compared to the simpler model with only excess Pd atoms in $4e$. With respect to the lack of other decisive methods, we assumed the simpler model throughout this paper. Tables II and III list the results of the refinement including interatomic distances (in Table III). It should be understood that in the present substitution mechanism a unit cell with In compensated by two Pd2 atoms will exclude the same substitution in the two adjacent unit cells along the z direction. This prevents unphysically short distances Pd2-Pd2 $=0.1459$ nm and Pd2-In $=0.1263$ nm.

The compositional dependence of the lattice parameters for the compounds located on branch A is similar to the

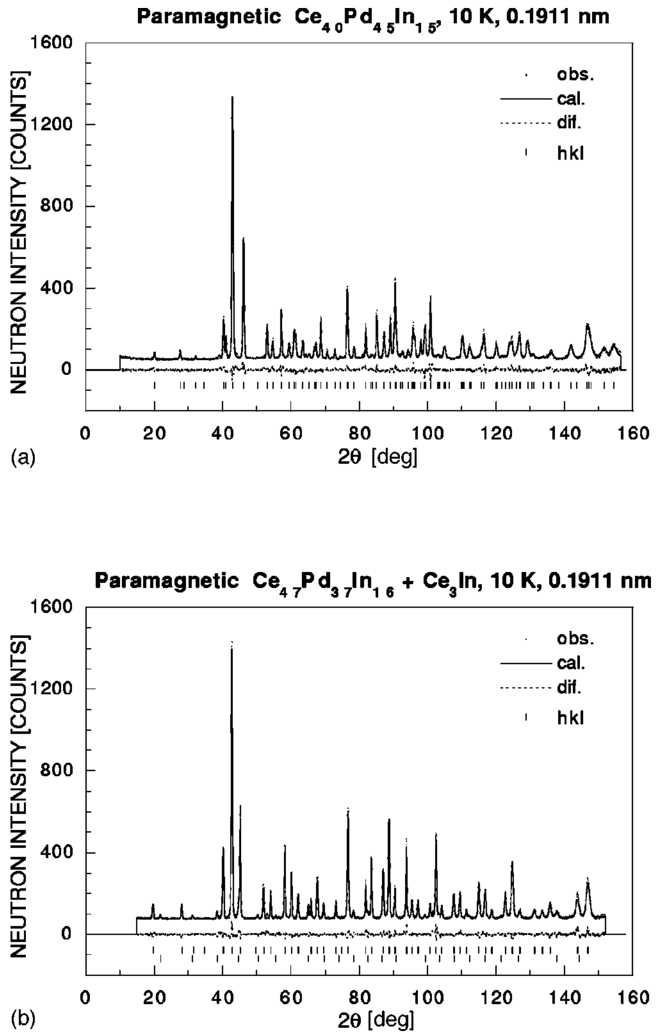

FIG. 2. Observed, calculated, and difference neutron-diffraction patterns of paramagnetic (a) $Ce_{40}Pd_{45}In_{15}$ (b) $Ce_{47}Pd_{37}In_{16}$ at $T=10$ K. The vertical bars at the bottom of (b) indicate Bragg peak positions for $Ce_{47}Pd_{37}In_{16}$ and Ce_3In, respectively.

analogous stannides and thus provokes the identical explanation.[7] With increasing occupation of the smaller Pd2 atoms at the $4e$ sites, instead of larger In at the $2a$ sites, the a parameter decreases, as expected, while the substitution of two Pd atoms for one In atom tends to expand the **c** axis (see Fig. 3 and Table I).

For the branch B of the τ solid solution, neutron-diffraction measurements on D1A were performed at $T=10$ K (in the paramagnetic state) for the alloy with the nominal composition $Ce_{47}Pd_{37}In_{16}$. This part of the alloy series is formed by a different mechanism compared to branch A. The excess of the bigger Ce atom (compared with the surplus of Pd in branch A) cannot be located in any interstitial position. Starting from the Mo_2FeB_2 type, we therefore propose a simple model where In atoms at the $2a$ site are replaced by Ce atoms. Apart from the dominant tetragonal phase, weak lines of Ce_3In are visible [see Fig. 2(b)] which are fitted by means of the program FULLPROF in the powder matching mode.[10] The volume fraction deduced for Ce_3In is about 4%. The structural results of the Rietveld profile fitting of the dominant phase are summarized in Table IV. Corresponding interatomic distances of Ce are listed in Table V.

TABLE II. Structural parameters of $Ce_{40}Pd_{45}In_{15}$ refined according to space group $P4/mbm$ from neutron-diffraction data taken at $T=10$ K. Overall isotropic temperature factor $B=0.59(2)\times10^{-2}$ nm^2, Occ. = occupation number, goodness of fit $\chi^2=3.94$, agreement R-Bragg factor $R_B=6.39\%$, agreement R-structure factor $R_F=5.17\%$, agreement value $R_{wp}=6.96\%$ concerning weigthed profile intensities, expected value from counting statistics $R_{exp}=3.51\%$, 88 inequivalent contributing reflections (hkl), * fixed. Estimated standard deviations are given within parentheses.

Atom	Site	x	y	z	Occ. [%]
Ce	$4h$	0.1753(1)	0.6753(1)	0.5	98(3)
Pd1	$4g$	0.3714(1)	0.8714(1)	0	100*
Pd2	$4e$	0	0	0.317(3)	14(3)
In	$2a$	0	0	0	86(3)

According to the radius ratio $R_{Ce}/R_{In}=0.180/0.166$ the simple In/Ce substitution directly leads to an increase of the a parameter with the c parameter staying almost constant. Searching for the crystal chemical differences between the two branches, a comparison of the interatomic distances reveals rather short Pd2-In distances $d_{Pd_2\text{-}In}=0.2722$ nm for branch A ($Ce_{1.95}Pd_{2+2x}In_{1-x}$) and short distances $d_{Ce_1\text{-}Ce_2}=0.3505$ nm in branch B ($Ce_{2+x}Pd_{1.85}In_{1-x}$). The remaining sublattices obviously behave indifferently.

Finally it can be observed that atom occupancies derived from the refinements are consistent with the composition evaluated by microprobe analysis for the branch A, where discrepancies are less than 1.5. at %. This difference has been accepted as possibly arising from measurement errors. For the branch B discrepancies for Ce and In, however, reach about 3–4 at. %. Assuming a similar reliability for the microprobe data, the explanation may lie in the poor neutron-scattering contrast of Ce and In atoms sharing the same site $2a$.

C. Magnetic properties

Magnetic susceptibility measurements were carried out for all the samples for both conditions (as cast and annealed) in order to investigate the effect of chemical micro-inhomogeneities on the magnetism. The $\chi_{ac}(T)$ for some of the as-cast samples resulted not in a simple peak, as it was always found in the case of annealed samples, but in more complicated behavior. This could be explained assuming that the as-cast samples have a propensity to be formed by regions of slightly different composition. Such a hypothesis is not unlikely because of the rather wide solid solubility range.

TABLE III. Interatomic distances (nm) in $Ce_{40}Pd_{45}In_{15}$ calculated from Table II.

Ce-2Pd1	0.2920	Ce-2Ce	0.3985
Ce-4Pd2	0.2932	Ce-4Ce	0.4017
Ce-4Pd1	0.3094	Pd1-Pd1	0.2799
Ce-4In	0.3469	Pd1-2In	0.3026
Ce-Ce	0.3817	Pd2-Pd2	0.2526
		Pd2-In	0.2722

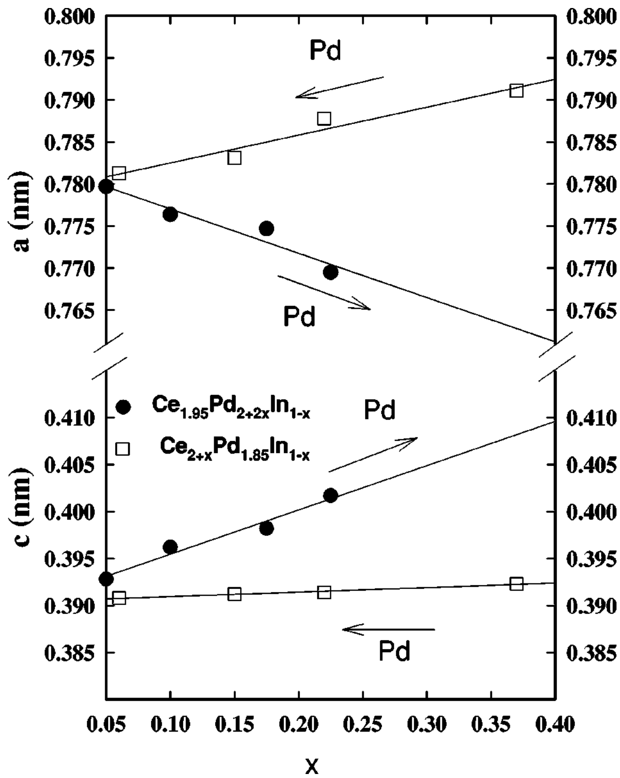

FIG. 3. The variation of the lattice parameters a and c at room temperature for the two branches $Ce_{1.95}Pd_{2+2x}In_{1-x}$ and $Ce_{2+x}Pd_{1.85}In_{1-x}$ of the τ solid solution, as a function of the composition x. The arrows labeled Pd indicate increasing amounts of this element in the two branches.

Corresponding to the two branches A and B, the magnetic behavior of the annealed samples can be divided into two subgroups. As an example for the common behavior of the samples located on branch B, the ac magnetic susceptibility of the annealed alloy with the nominal composition $Ce_{50}Pd_{36}In_{14}$ is shown in Fig. 4(a). A pronounced maximum both in the real and in the imaginary component of χ_{ac} indicates that the compound orders ferromagnetically below $T_C = 3.8$ K. The magnetization measured at 2 K as a function of the applied field for the samples $Ce_{45}Pd_{35}In_{20}$, $Ce_{47}Pd_{37}In_{16}$, and $Ce_{50}Pd_{36}In_{14}$ is displayed in Fig. 5(a). The magnetization reaches in a field of 0.5 T already about 70% of the value reached at 6 T, although it continues slightly to rise with increasing field. Moreover the magnetic moments obtained for the three samples at 6 T $\mu(6\ \mathrm{T},\ 2\ \mathrm{K}) = 0.88\mu_B$/Ce atom, $\mu(6\ \mathrm{T},\ 2\ \mathrm{K}) = 0.83\mu_B$/Ce atom, $\mu(6\ \mathrm{T},\ 2\ \mathrm{K}) = 0.80\mu_B$/Ce atom, attain only about 40% of the saturation moment of the free Ce^{+3} ion, presumably due to crystal-field effects. Finally, Kondo interactions may give rise to a further reduction of the ordered magnetic moments in the respective crystal-field ground state.

Figure 4(b) displays the ac susceptibility of the sample with the nominal composition $Ce_{40}Pd_{45}In_{15}$, located at the Pd-rich branch A. Differently from Fig. 4(a), here only the real component of the ac susceptibility shows a maximum, while the imaginary part does not follow this trend. This fact indicates that the $Ce_{40}Pd_{45}In_{15}$ compound orders antiferromagnetically below $T_N = 4$ K. Magnetization data $M(T)$ taken at different magnetic fields are shown in Fig. 6. For very low fields a maximum at $T = 4$ K confirms the antiferromagnetic behavior of this compound. For rising values of the magnetic field the maximum is shifted to lower temperatures and below about 3 K there is a gradual tendency for the magnetization to increase again as the temperature decreases. At $\mu_0 H = 1$ T, the antiferromagnetic order is washed out and the magnetization rises monotonically. This behavior

TABLE IV. Structural parameters of $Ce_{47}Pd_{37}In_{16}$ refined according to space group $P4/mbm$ from neutron-diffraction data taken at $T = 10$ K. Overall isotropic temperature factor $B = 0.55(3) \times 10^{-2}$ nm^2, Occ. = occupation number, goodness of fit $\chi^2 = 3.14$, agreement R-Bragg factor $R_B = 4.87\%$, agreement R-structure factor $R_F = 3.36\%$, agreement value $R_{wp} = 4.98\%$ concerning weighted profile intensities, expected value from counting statistics $R_{exp} = 2.81\%$, 91 inequivalent contributing reflections (hkl), * fixed. Estimated standard deviations are given within parentheses.

Atom	Site	x	y	z	Occ.[%]
Ce1	4h	0.1730(1)	0.6730(1)	0.5	100*
Pd	4g	0.3718(1)	0.8718(1)	0	100(3)
Ce2	2a	0	0	0	40(3)
In	2a	0	0	0	60(3)

TABLE V. Interatomic distances (nm) in $Ce_{47}Pd_{37}In_{16}$ calculated from Table IV.

Ce1-2Pd	0.2952	Ce1-2Ce1	0.3922
Ce1-4Pd	0.3093	Pd-Pd	0.2849
Ce1-4(Ce2/In)	0.3505	Pd-2(Ce2/In)	0.3088
Ce1-Ce1	0.3842	Pd-2Pd	0.3922

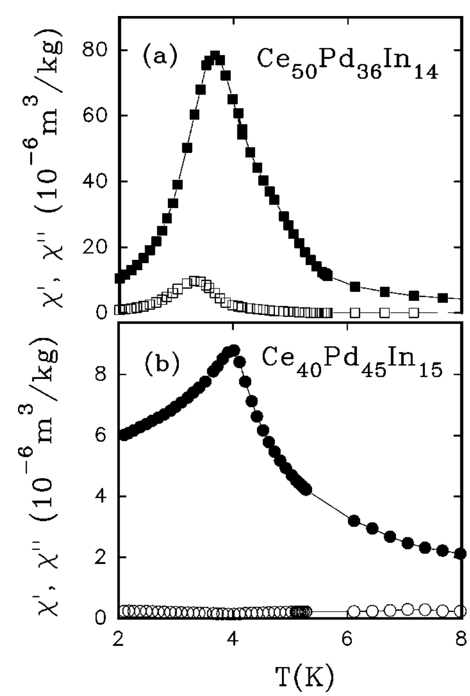

FIG. 4. Real and imaginary component of ac magnetic susceptibility for (a) $Ce_{50}Pd_{36}In_{14}$ and (b) $Ce_{40}Pd_{45}In_{15}$.

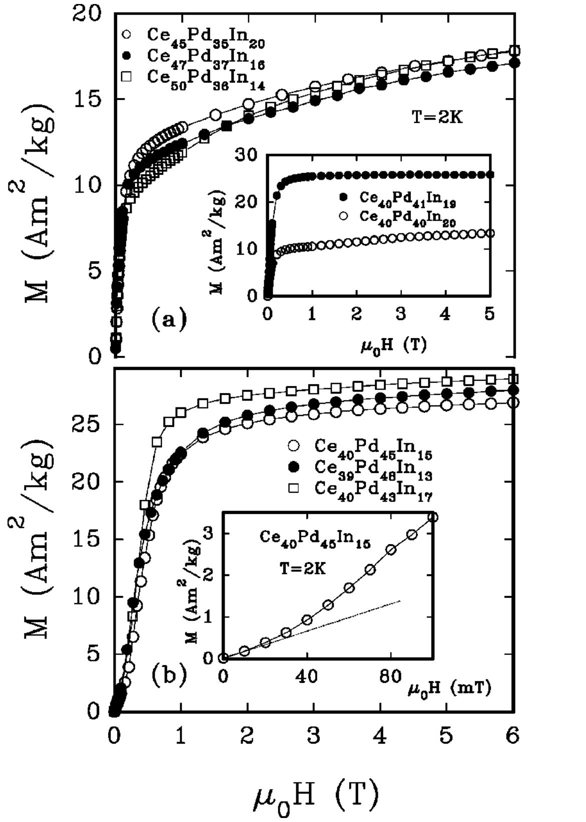

FIG. 5. Field dependence of the magnetization measured at 2 K for (a) $Ce_{45}Pd_{35}In_{20}$, $Ce_{47}Pd_{37}In_{16}$, and $Ce_{50}Pd_{36}In_{14}$. The inset displays the magnetization for $Ce_{40}Pd_{40}In_{20}$ and $Ce_{40}Pd_{41}In_{19}$ as a function of the applied magnetic field (b) $Ce_{40}Pd_{45}In_{15}$, $Ce_{39}Pd_{48}In_{13}$, and $Ce_{40}Pd_{43}In_{17}$. In the inset is shown the field dependence of the magnetization at low field for $Ce_{40}Pd_{45}In_{15}$. The dashed line displays a straight-line behavior of $M(H)$ below about 15 mT.

strongly suggests a spin-flip effect in which the antiferromagnetic order is converted to a ferromagnetic order by the magnetic field. This is in line with the isothermal magnetization at 2 K [see inset of Fig. 5(b)] which exhibits a metamagnetic transition for fields above 15 mT. The magnetization reaches at low fields a saturation value, which at 2 K and

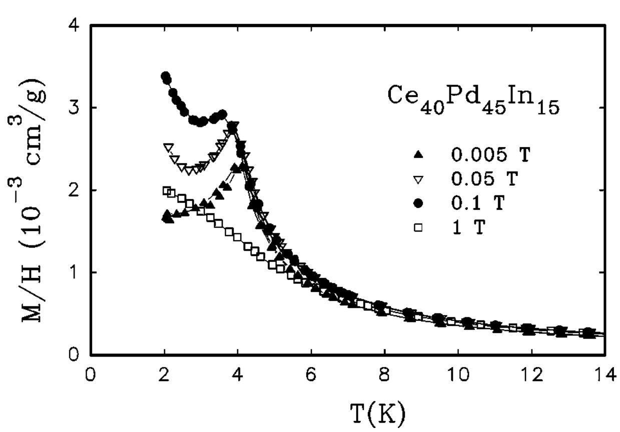

FIG. 6. Temperature dependence of the magnetization for $Ce_{40}Pd_{45}In_{15}$ measured in the external magnetic fields 0.005, 0.05, 0.1, and 1 T.

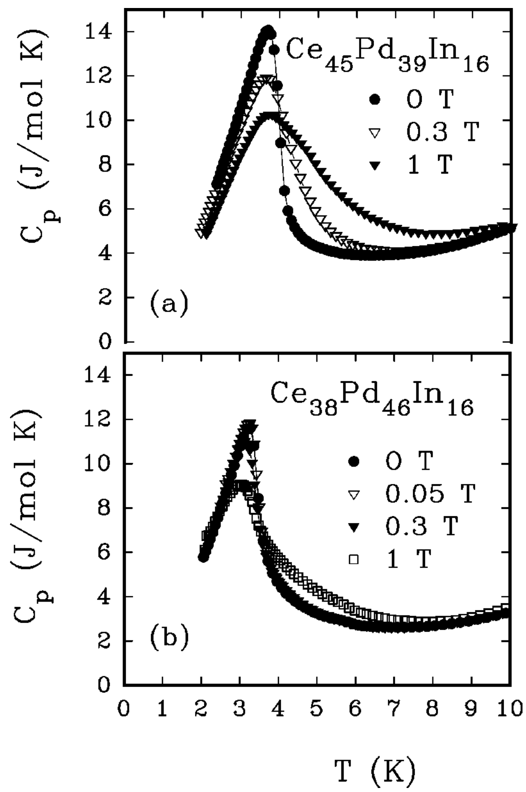

FIG. 7. Specific heat (C_p) measured in external magnetic field, as a function of temperature of (a) $Ce_{45}Pd_{39}In_{16}$ and (b) $Ce_{38}Pd_{46}In_{16}$.

6 T is $1.38\mu_B$/Ce atom, larger than for the ferromagnetic compound but still well below the saturation value for the free Ce^{+3} ion ($2.54\mu_B$).

The different magnetization processes between samples located on branch A and B are obvious from a comparison of Figs. 5(a) and 5(b). On the Pd-rich branch A with the modulated antiferromagnetic ground state, the magnetization approches saturation above the metamagnetic transition already at modest fields (4–6 T), while for the ferromagnetic compounds on the Ce-rich branch B a magnetic field of 22 T would be required to reach the ''saturation'' ($\sim$28 A m^2/kg). Actually this variation occurs already close to the ''virtual'' crossover of the two branches as is shown in the inset of Fig. 5(a), which compares the magnetization curves of the 2 alloys prepared with the nominal composition close to each other $Ce_{40}Pd_{40}In_{20}$ and $Ce_{40}Pd_{41}In_{19}$. Through the crossover from the Pd-rich to the Ce-rich branch the magnetization is reduced by nearly a factor of two and an appreciable anisotropy occurs which may be attributed to the structural change due to a tiny variation of the stoichiometry. It should be mentioned that the magnetic data published previously for the ''stoichiometric'' composition Ce_2Pd_2In[4] match perfectly with the antiferromagnetic data revealed for $Ce_{40}Pd_{41}In_{19}$ as part of branch B of the two solid solution ranges.

Figures 7(a) and 7(b) display typical low-temperature specific-heat measurements performed at different magnetic fields on $Ce_{38}Pd_{46}In_{16}$ and $Ce_{45}Pd_{39}In_{16}$ situated at branch A and branch B, respectively. A comparison of both figures reveals that the magnetic fields applied to $Ce_{45}Pd_{39}In_{16}$ shifts the λ-like anomaly in $C_p(T)$ to higher temperatures and additionally the maximum becomes significantly broader. Such a behavior is typically found for ferromagnetic materials, in agreement with the susceptibility data. On the contrary, the λ-like anomaly found in $C_p(T)$ for $Ce_{38}Pd_{46}In_{16}$ is reduced in both the temperature and the jump height ΔC as the magnetic-field strength increases. This particular behavior is a typical feature of antiferromagnetically ordered systems.

To estimate the Kondo temperatures from the specific-heat measurements of these alloys, we used a procedure discussed in detail by Besnus *et al.*,[14] which is based on the model of Schotte and Schotte[15]. In the mean-field approximation, the jump ΔC of the specific heat at $T=T_{mag}$ is related with to the ratio of the Kondo temperature T_K and the ordering temperature $T_{C,(N)}$ by

$$\Delta C=\frac{6R}{\psi'''(1/2+\zeta)}[\psi'(1/2+\zeta)+\zeta\psi''(1/2+\zeta)]^2 \qquad (1)$$

with $\zeta=(T_K/T_{C,(N)})/2\pi$ and ψ', ψ'', and ψ''' are the first three derivatives of the digamma function. This analysis yields $T_K=0.8$ and 1.2 K for the ferromagnetic and the antiferromagnetic alloy, respectively. In both cases the Kondo interaction strength is relatively weak and the reduction of the ordered moments due to Kondo screening is expected to be small, too.

D. Ferromagnetism of $Ce_{47}Pd_{37}In_{16}$

The difference pattern of the neutron intensities measured at $T=1.6$ K and $T=10$ K for $Ce_{47}Pd_{37}In_{16}$ is shown in Fig. 8(a). Pure ferromagnetic order for this compound is confirmed since the neutron-diffraction intensity at 1.6 K exhibits no additional reflections in comparison with that at 10 K (nuclear pattern) and the magnetic scattering intensity is superimposed on nuclear peaks only. In our model of the chemical structure, which is summarized in Table IV, Ce occupies both $4h$ sites and, to 40%, In $2a$ sites. This is also essential to obtain the good fit ($\chi^2=1.2$, agreement value $R_{IM}=9.9\%$ concerning integrated magnetic neutron intensities) shown in Fig. 8(a). The corresponding ordered magnetic moments μ are oriented parallel to the direction [0,0,1]. At 1.6 K $\mu_{Ce(4h)}=1.25(4)\mu_B$ and $\mu_{Ce(2a)}=0.9(2)\mu_B$, respectively. Figure 8(b) shows the thermal dependence of the magnetic moment as deduced from the temperature dependence of the (210) peak normalized to the $T=1.6$ K value. This curve indicates a second-order phase transition at the Curie point T_C of approximately 4.0(2) K. It is worth noting that there is a good agreement between the magnetization calculated from these values referred to the unit cell ($M_{U.C.}=5.72\mu_B$) and the saturated magnetization of the samples on branch B ($M_{U.C}\approx 5.9\mu_B$).

As already mentioned above, the reduction of the magnetic moments with respect to the free Ce^{+3} ion follows primarily from crystal-field splitting of the $j=5/2$ state exposed to the crystalline electric field in tetragonal symmetry and, to a much smaller extent, from the Kondo effect. Without knowledge of the particular crystal-field level scheme, it is impossible to assign the observed moment to a certain crystal-field ground-state wave function. In any case, however, the ground state of $Ce_{47}Pd_{37}In_{16}$ is not primarily governed from the $|\pm 1/2\rangle$ state. Most significant is the tail of the

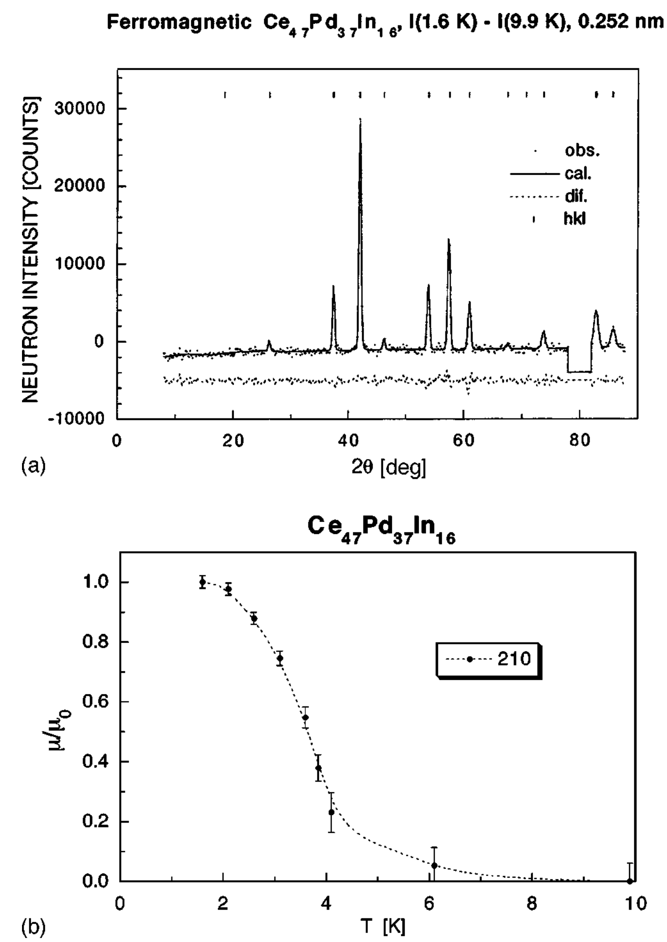

FIG. 8. (a) Magnetic pattern of the neutron intensity with the Rietveld profile fitting for the ferromagnetic $Ce_{47}Pd_{37}In_{16}$ sample. (b) Temperature dependence of the reduced ferromagnetic Ce moment of $Ce_{47}Pd_{37}In_{16}$ (relative units, since there are two Ce sites with different moments).

magnetic intensity above the ferromagnetic transition temperature as determined from the magnetic susceptibility or the temperature-dependent specific heat. Most likely, this tail originates from short-range magnetic order effects above T_C or from magnetic inhomogeneities of the polycrystalline sample.

E. Antiferromagnetism of $Ce_{40}Pd_{45}In_{15}$

Excess Pd atoms in $Ce_{40}Pd_{45}In_{15}$ occupy $4e$ sites: (0,0, $\simeq 0.32$), similar to the homologous stannide compounds.[7] As shown in Fig. 9(a), $Ce_{40}Pd_{45}In_{15}$ orders antiferromagnetically according to a rather puzzling magnetic difference neutron-diffraction pattern. With profile matching[10] we obtained best fits with $\mathbf{k}\simeq[0.22,0,0]$ similarly to the Sn compound.[6]

1. Symmetry analysis

Based on the information on the **k** vector, we started a group-theoretical symmetry analysis of the magnetic ordering by means of the program MODY (Ref. 16) for space group $P4/mbm$. For the given **k** vector and the set of four Ce atoms ($4h$), there are four one-dimensional, complex irreducible representations τ_β. The corresponding basic axial vector modes ${}^{\alpha}\boldsymbol{\Psi}_{\beta\gamma\delta}$ related to the irreducible representations τ_β

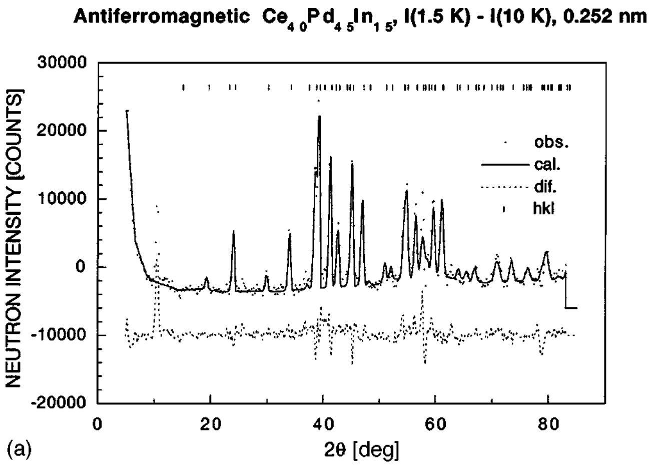

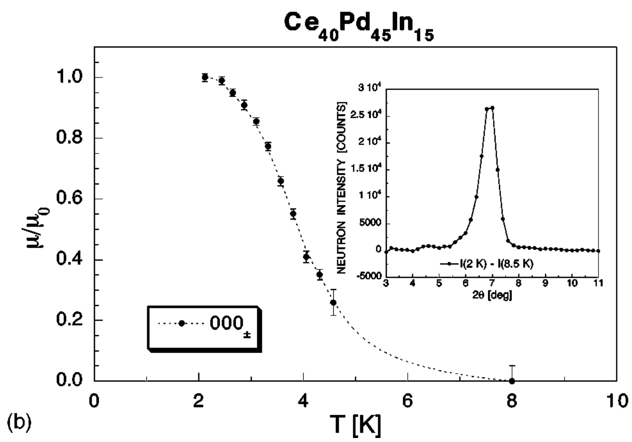

FIG. 9. (a) Magnetic pattern of the neutron intensity with the Rietveld profile fitting for the antiferromagnetic $Ce_{40}Pd_{45}In_{15}$ sample. (b) Reduced antiferromagnetic Ce moment of $Ce_{40}Pd_{45}In_{15}$ versus temperature (normalized to $\mu_0 = 1.7\mu_B$ at 1.6 K). Inset: Intense antiferromagnetic $000_\pm$ satellite, observed on DMC with neutron wavelength $\lambda_n = 0.420$ nm.

are summarized in Table VI. The magnetic representation decomposes into two orbits, corresponding with three magnetic moment components for four atoms to 12 degrees of freedom:

$$\tau_I(6) = \tau_1(1) + 2\tau_2(1) + 2\tau_3(1) + \tau_4(1);$$

$$\tau_{II}(6) = \tau_1(1) + 2\tau_2(1) + 2\tau_3(1) + \tau_4(1).$$

This implies that there are only symmetry relations between atoms 1, 2 and 3, 4, respectively. As the irreducible representations are complex, one has to find suitable linear combinations of the magnetic modes ${}^{\alpha}\boldsymbol{\Psi}_{\beta\gamma\delta}(\mathbf{r}_j)$ for the wave vectors $\mathbf{k}$ and $-\mathbf{k}$, in order to get real models of the magnetic structure. Apart from the arms α of the star of the $\mathbf{k}$ vector, one should consider for this sum the different irreducible representations β and their ''dimensions'' (index δ). $\mathbf{r}_j$ denotes the position of a magnetic ion of an orbit γ. The coefficients in the linear combinations define the order parameters. As the magnetic moments of the atoms in the nth chemical unit cell are related by $e^{i\mathbf{k}\mathbf{t}_n}$ to the 0th unit cell via the basic translations $\mathbf{t}_n$,[17] we may restrict ourselves to the four Ce atoms in the chemical unit cell.

Considering the easy direction of magnetization [0,0,1] in ferromagnetic $Ce_{47}Pd_{37}In_{16}$, we may assume this also for antiferromagnetic $Ce_{40}Pd_{45}In_{15}$. This implies that we have to consider only representations τ_1 and τ_4 in Table VI. Due to the decomposition into two orbits, one has the freedom of two different amplitudes (A, B) and phases (φ,ψ). Thus we choose the order parameters $p_1 = (Av/2, -Bu^2w^*/2)$ and $p_2 = (Bw/2, -Au^2v^*/2)$ for the orbits 1 and 2, respectively, where the first term in the bracket refers to $\mathbf{k} = \mathbf{k}_4$ and the second to $\mathbf{k}_3$ being equivalent to $-\mathbf{k}_4$, $v = e^{i\varphi}$, $w = e^{i\psi}$. This yields for the irreducible representation τ_4 and the four sites given in Table VI:

$$\mathbf{S}(1+n) = A\mathbf{e}_z \cos(\mathbf{k}_4\mathbf{t}_n - \pi q + \varphi),$$

$$\mathbf{S}(2+n) = A\mathbf{e}_z \cos(\mathbf{k}_4\mathbf{t}_n + \varphi),$$

$$\mathbf{S}(3+n) = B\mathbf{e}_z \cos(\mathbf{k}_4\mathbf{t}_n - \pi q + \psi),$$

$$\mathbf{S}(4+n) = B\mathbf{e}_z \cos(\mathbf{k}_4\mathbf{t}_n + \psi),$$

where $\mathbf{S}(j+n)$ represents the magnetic moment at site $\mathbf{r}_j$ in the chemical unit cell n, and $\mathbf{e}_z$ is a unit vector along the z direction. The phase difference $-\pi q$ between sites 1, 2 and 3, 4, respectively, is caused by the translational difference $\mathbf{a}/2$. For τ_1 the difference is only a change of sign among $\mathbf{S}(1+n)$ and $\mathbf{S}(3+n)$.

2. Antiferromagnetic structure

Using the previously discussed symmetry analysis we started refinements of the neutron-diffraction data by means of the program FULLPROF.[10] As a common phase shift cannot be detected from the magnetic neutron intensities, we assign $\varphi = 0$. Indeed the best fit of the magnetic structure—shown in Fig. 9(a)—was obtained for the modulated magnetic structure according to the irreducible representation τ_4 with goodness of fit $\chi^2 = 4.3$ and $R_{IM} = 15.2\%$ concerning integrated magnetic neutron intensities, which is satisfactory in view of the rather complicated magnetic difference neutron-diffraction pattern. Practically the same magnetic moment amplitude $A_{\mu(Ce)} = 1.7(1)\mu_B$ $(\boldsymbol{\mu}\|[0,0,1])$ resulted for both groups of Ce atoms 1, 2 and 3, 4. The phase ψ was refined to 0.063(3), in units of 2π and q to 0.217(1), respectively. The modulation of the four Ce magnetic moments along the $\mathbf{a}$ axis according to the propagation vector (0.22,0,0) is shown in Fig. 10.

An antiferromagnetic configuration according to the irreducible representation τ_1 yielded very bad fits (χ^2 of the order of 82). The peak around $2\Theta = 10°$ in Fig. 9(a) is either caused by an impurity phase or due to another $\mathbf{k}$ vector, e.g., associated with a higher harmonic in the sense of a Fourier expansion. The latter is more probable as the neutron-diffraction measurements performed on D1B (with $\lambda = 0.252$ nm) showed that this peak disappears approximately at the same temperature as the other magnetic reflections. However, single-crystal investigations would be required to clearly identify such generally weaker higher harmonics. The considerable increase of the ''background'' which is illustrated in Fig. 9(a) at low scattering angles, is partially caused by a very intense satellite peak $000_\pm$ which at the time of the

TABLE VI. Possible magnetic modes for space group $P4/mbm$ (no. 127) in case of R 4h sites: $(x,x+1/2,1/2)$; $(x+1/2,\bar{x},1/2)$; $(\bar{x}+1/2,x,1/2)$; $(\bar{x},\bar{x}+1/2,1/2)$, $x\simeq 0.17$ of R_2Pd_2In for propagation vectors $\mathbf{k}_4$ and $\mathbf{k}_3$, which is equivalent to $-\mathbf{k}_4$, as obtained by program MODY (Ref. 16). τ = irreducible representation, wave vectors: $\mathbf{k}_1=[0,q,0]$, $\mathbf{k}_2=[0,1-q,0]$, $\mathbf{k}_3=[1-q,0,0]$, $\mathbf{k}_4=[q,0,0]$, $u=e^{i\pi q}$, $q\approx 0.22$.

$(4h)$ site:	mode	1: (0.17,0.67,1/2)	2: (0.67,0.83,1/2)	3: (0.33,0.17,1/2)	4: (0.83,0.33,1/2)
τ_1:					
$\mathbf{k}_4$, orbit 1	${}^4\mathbf{\Psi}_{111}$	$(0,0,-u^*)$	(0,0,1)		
$\mathbf{k}_3$, orbit 1	${}^3\mathbf{\Psi}_{111}$			$(0,0,u^*)$	$(0,0,-u^{*2})$
$\mathbf{k}_4$, orbit 2	${}^4\mathbf{\Psi}_{121}$			$(0,0,-u^*)$	(0,0,1)
$\mathbf{k}_3$, orbit 2	${}^3\mathbf{\Psi}_{121}$	$(0,0,u^*)$	$(0,0,-u^{*2})$		
τ_2:					
$\mathbf{k}_4$, orbit 1	${}^4\mathbf{\Psi}_{211}$	$(0,u^*,0)$	$(0,-1,0)$		
$\mathbf{k}_4$, orbit 1	${}^4\mathbf{\Psi}_{212}$	$(u^*,0,0)$	(1,0,0)		
$\mathbf{k}_3$, orbit 1	${}^3\mathbf{\Psi}_{211}$			$(0,u^*,0)$	$(0,-u^{*2},0)$
$\mathbf{k}_3$, orbit 1	${}^3\mathbf{\Psi}_{212}$			$(-u^*,0,0)$	$(-u^{*2},0,0)$
$\mathbf{k}_4$, orbit 2	${}^4\mathbf{\Psi}_{221}$			$(0,u^*,0)$	$(0,-1,0)$
$\mathbf{k}_4$, orbit 2	${}^4\mathbf{\Psi}_{222}$			$(u^*,0,0)$	(1,0,0)
$\mathbf{k}_3$, orbit 2	${}^3\mathbf{\Psi}_{221}$	$(0,u^*,0)$	$(0,-u^{*2},0)$		
$\mathbf{k}_3$, orbit 2	${}^3\mathbf{\Psi}_{222}$	$(-u^*,0,0)$	$(-u^{*2},0,0)$		
τ_3:					
$\mathbf{k}_4$, orbit 1	${}^4\mathbf{\Psi}_{311}$	$(0,-u^*,0)$	$(0,-1,0)$		
$\mathbf{k}_4$, orbit 1	${}^4\mathbf{\Psi}_{312}$	$(-u^*,0,0)$	(1,0,0)		
$\mathbf{k}_3$, orbit 1	${}^3\mathbf{\Psi}_{311}$			$(0,-u^*,0)$	$(0,-u^{*2},0)$
$\mathbf{k}_3$, orbit 1	${}^3\mathbf{\Psi}_{312}$			$(u^*,0,0)$	$(-u^{*2},0,0)$
$\mathbf{k}_4$, orbit 2	${}^4\mathbf{\Psi}_{321}$			$(0,-u^*,0)$	(0,-1,0)
$\mathbf{k}_4$, orbit 2	${}^4\mathbf{\Psi}_{322}$			$(-u^*,0,0)$	(1,0,0)
$\mathbf{k}_3$, orbit 2	${}^3\mathbf{\Psi}_{321}$	$(0,-u^*,0)$	$(0,-u^{*2},0)$		
$\mathbf{k}_3$, orbit 2	${}^3\mathbf{\Psi}_{322}$	$(u^*,0,0)$	$(-u^{*2},0,0)$		
τ_4:					
$\mathbf{k}_4$, orbit 1	${}^4\mathbf{\Psi}_{411}$	$(0,0,u^*)$	(0,0,1)		
$\mathbf{k}_3$, orbit 1	${}^3\mathbf{\Psi}_{411}$			$(0,0,-u^*)$	$(0,0,-u^{*2})$
$\mathbf{k}_4$, orbit 2	${}^4\mathbf{\Psi}_{421}$			$(0,0,u^*)$	(0,0,1)
$\mathbf{k}_3$, orbit 2	${}^3\mathbf{\Psi}_{421}$	$(0,0,-u^*)$	$(0,0,-u^{*2})$		

D1B measurements was not detected $[2\Theta_{cal.}\approx 4.1(2)°]$. As it should be there according to the calculation, we investigated $Ce_{40}Pd_{45}In_{15}$ on DMC at SINQ with 0.42 nm neutrons. As illustrated in Fig. 9(b), the $000_{\pm}$ peak clearly exists. Moreover, Table VII indicates reasonable agreement between the observed and the calculated [from the model of Fig. 9(a)] magnetic integrated neutron intensities. It should be noted that the position of this peak does not show a significant change with temperature [at $T=2.1$ K: $2\Theta_{obs.}=6.87(1)°$, at $T=3.6$ K: $2\Theta_{obs.}=6.83(2)°$, at $T=4.3$ K: $2\Theta_{obs.}=6.80(5)°$], i.e., the period of the modulation is practically constant. Figure 9(b) indicates a second-order phase transition at a Néel temperature of approximately 4.0(2) K.

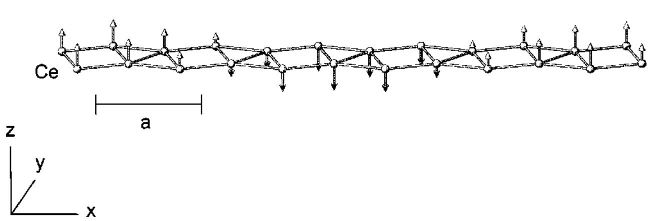

FIG. 10. Sinusoidal modulation in $Ce_{40}Pd_{45}In_{15}$ of the four Ce magnetic moments along the **a** axis with a period of about 4.55 **a** lattice vectors.

IV. CONCLUSIONS

The solid solubility range of the ternary compound Ce_2Pd_2In with the parent Mo_2FeB_2 chemical structure (space group $P4/mbm$) was investigated by microprobe analysis, *x*-ray and neutron diffraction, as well as by magnetic measurements to elucidate the influence of the chemical composition on the magnetic ground state. The complex substitutional mechanisms could be resolved to a great extent

TABLE VII. Comparison between observed and calculated integrated intensities of $Ce_{40}Pd_{45}In_{15}$ at $T=2$ K for neutron wavelength $\lambda=0.42$ nm (DMC measurement).

$2\Theta_{cal.}$ [deg]	$2\Theta_{obs.}$ [deg]	$h\pm q,k,l$	$I_{cal.}$	$I_{cal.,scaled}$	$I_{obs.}$	$I_{\Delta obs.}$
6.8	6.9	$000_{\pm}$	449460	19563	21040	435
40.5	40.7	110_{-}	1549	67	63	13
66.6	66.6	$020_{\pm}$	3715	162	118	14
67.8	67.8	210_{-}	6124	267	277	17
71.7	71.7	120_{-}	4429	193	143	13
74.4	74.6	200_{+}	1989	87	62	17
79.4	79.4	120_{+}	4618	201	201	17

yielding two branches $Ce_{1.95}Pd_{2+2x}In_{1-x}$ $(0.05\leq x\leq 0.23)$ and $Ce_{2+x}Pd_{1.85}In_{1-x}$ $(0.06\leq x\leq 0.37)$ for the τ solid solution. In the Pd-rich branch In vacancies at the $2a$ site are compensated by a surplus of Pd located at an additional $4e$ site, whereas an excess of Ce replaces In at the $2a$ site in the Ce-rich branch. The latter branch gives rise to a ferromagnetic ground state while in the former incommensurate antiferromagnetism occurs, which is clearly resolved in the heat capacity and magnetic measurements. The bulk measurements are confirmed by the present neutron-diffraction experiments with the important findings that the surplus of Pd compared to the Ce_2Pd_2In stoichiometry favours antiferromagnetism of a sinusoidal modulated type with the propagation vector $\mathbf{k}\approx[0.22,0,0]$, whereas the excess of Ce induces ferromagnetism. This remarkable change of magnetic ordering is presumably caused by differences in crystal-field and Ruderman-Kittel-Kasuya-Yosida exchange interactions associated with the alterations of the coordination of the Ce^{3+} ions. The ordered magnetic moments of Ce at saturation: $\mu_{ferro}\leq 1.3\mu_B$ and $\mu_{antiferro}\leq 1.7\mu_B$ indicate significant crystal-field and in minor extent Kondo reductions below the free ion value of $2.14\mu_B$ of Ce^{3+} with $^2F_{5/2}$ ground-state multiplet. On the other hand, the ordering temperatures T_C and T_N appear to be practically identical within the precision of the present neutron-diffraction data.

ACKNOWLEDGMENTS

The research reported herein was supported by the Austrian National Science Foundation FWF under Grant Nos. P13544 and P9709, as well as by the Swiss National Science Foundation, which are most gratefully acknowledged. Some of the authors, M.G., P.R., A.S., and R.F., are also grateful to the Italian-Austrian Scientific-Technological Exchange Program for supporting research in Genova and Wien, respectively (Project No. N26). Special thanks are due to the officials of the Italian Foreign Affair Ministry and the Italian Embassy in Wien.

[1] F. Hulliger and B.Z. Xue, J. Alloys Compd. **215**, 267 (1994).
[2] S. Mock, A. Faisst, H. v. Lohneysen, Phys. Rev. B **56**, 335 (1997).
[3] R.A. Gordon, Y. Ijiri, C.M. Spencer, and F.J. DiSalvo, J. Alloys Compd. **224**, 101 (1995).
[4] D. Kaczorowski, P. Rogl, and K. Hiebl, Phys. Rev. B **54**, 9891 (1996).
[5] D. Kaczorowski, M. Giovannini, R. Hauser, H. Michor, E. Bauer, and G. Hilscher, Czech. J. Phys. **46**, 2063 (1996).
[6] D. Laffargue, F. Fourgeot, F. Bourée, B. Chevalier, T. Roisnel, and J. Etourneau, Solid State Commun. **100**, 575 (1996).
[7] F. Fourgeot, P. Gravereau, B. Chevalier, L. Fournes, and J. Etourneau, J. Alloys Compd. **238**, 102 (1996).
[8] R.A. Gordon and F.J. DiSalvo, J. Alloys Compd. **238**, 57 (1996).
[9] M. Giovannini, H. Michor, E. Bauer, G. Hilscher, P. Rogl, and R. Ferro, J. Alloys Compd. **280**, 26 (1998).
[10] J. Rodriguez-Carvajal, Physica B **192**, 55 (1993).
[11] A.J. Freeman and J.P. Desclaux, J. Magn. Magn. Mater. **12**, 11 (1979).
[12] M. Giovannini *et al.* (unpublished).
[13] R. Mallik, E.V. Sampathkumaran, J. Dumshat, and G. Wortmann, Solid State Commun. **102**, 59 (1997).
[14] M. J. Besnus, A. Braghta, N. Hamdaoui, and A. Meyer, J. Magn. Magn. Mater. **104-107**, 1385 (1992).
[15] K. D. Schotte and U. Schotte, Phys. Lett. **55A**, 38 (1975).
[16] W. Sikora, in *Symmetry and Structural Properties of Condensed Matter*, edited by T. Lulek, B. Lulek, and M. Kuzma (World Scientific, Singapore, 1999), p. 484.
[17] Yu.A. Izyumov and V.E. Naish, J. Magn. Magn. Mater. **12**, 239 (1979).